Geophysical Journal International

Geophys. J. Int. (2014) **196,** 1869–1877
Advance Access publication 2014 January 13

doi: 10.1093/gji/ggt502

Resolution of non-double-couple components in the seismic moment tensor using regional networks—I: a synthetic case study

Eva Stierle,[1] Vaclav Vavryčuk,[2] Jan Šílený[2] and Marco Bohnhoff[1,3]

[1] *Helmholtz-Centre, Potsdam German Research Centre for Geosciences (GFZ), Telegrafenberg, D-*14473 *Potsdam, Germany. E-mail: stierle@gfz-potsdam.de*
[2] *Institute of Geophysics, Academy of Sciences of the Czech Republic, Bocni II/*1401*, Cz-*14131 *Prague, Czech Republic*
[3] *Department of Earth Sciences, Free University Berlin, Malteser Strasse* 74-100*, D-*12249 *Berlin, Germany*

Accepted 2013 December 8. Received 2013 December 8; in original form 2013 April 10

SUMMARY

We perform a detailed synthetic study on the resolution of non-double-couple (non-DC) components in the seismic moment tensors from short-period data observed at regional networks designed typically for monitoring aftershock sequences of large earthquakes. In addition, we test two different inversion approaches—a linear full moment tensor inversion and a non-linear moment tensor inversion constrained to a shear-tensile source model. The inversions are applied to synthetic first-motion *P*- and *S*-wave amplitudes, which mimic seismic observations of aftershocks of the 1999 $M_w = 7.4$ Izmit earthquake in northwestern Turkey adopting a shear-tensile source model. To analyse the resolution capability for the obtained non-DC components inverted, we contaminate synthetic amplitudes with random noise and incorporate realistic uncertainties in the velocity model as well as in the hypocentre locations. We find that the constrained moment tensor inversion yields significantly smaller errors in the non-DC components than the full moment tensor inversion. In particular, the errors in the compensated linear vector dipole (CLVD) component are reduced if the constrained inversion is applied. Furthermore, we show that including the *S*-wave amplitudes in addition to *P*-wave amplitudes into the inversion helps to obtain reliable non-DC components. For the studied station configurations, the resolution remains limited due to the lack of stations with epicentral distances less than 15 km. Assuming realistic noise in waveform data and uncertainties in the velocity model, the errors in the non-DC components are as high as ±15 per cent for the isotropic and CLVD components, respectively, thus being non-negligible in most applications. However, the orientation of *P*- and *T*-axes is well determined even when errors in the modelling procedure are high.

Key words: Inverse theory; Numerical approximations and analysis; Earthquake source observations; Theoretical seismology.

1 INTRODUCTION

Recent progress in seismic monitoring technology resulted in waveform recordings allowing detailed studies on the earthquake rupture process. In that respect, one of the key objectives is to resolve reliable non-shear components in the seismic moment tensors and to assess their resolution. Since it is known that brittle damage is expected to produce generically some tensile component of faulting (Ben-Zion & Ampuero 2009), the approximation of a shear slip on a planar fault, represented by a double-couple (DC) source model, seems to be too simple for some types of seismicity such as volcanic or geothermal earthquakes. Earthquake rupture processes might involve significant amounts of non-DC components, such as tensional components in the source mechanism (see, e.g. Frohlich 1994; Julian *et al*. 1998; Miller *et al*. 1998; Horálek *et al*. 2002; Rößler *et al*. 2007; Minson *et al*. 2007). However, observed non-DC components can also be artificial reflecting errors in the modelling procedure, seismic noise or a lack of data, for example, due to sparse distribution of stations on the focal sphere (Kravanja *et al*. 1999; Rößler *et al*. 2008; Šílený 2009). In this respect, one principal but yet less addressed objective is estimating the accuracy and reliability of the source related non-DC components of retrieved seismic moment tensors. Specifically it is important to know, if and how accurately the non-DC components can be resolved for a given station configuration under certain conditions, such as seismic noise level and inaccurate information on the velocity structure. Therefore, it is desirable to quantify a confidence level above which non-DC components can be considered to be statistically significant (Panza & Sarao 2000) prior to any analysis of field observations.

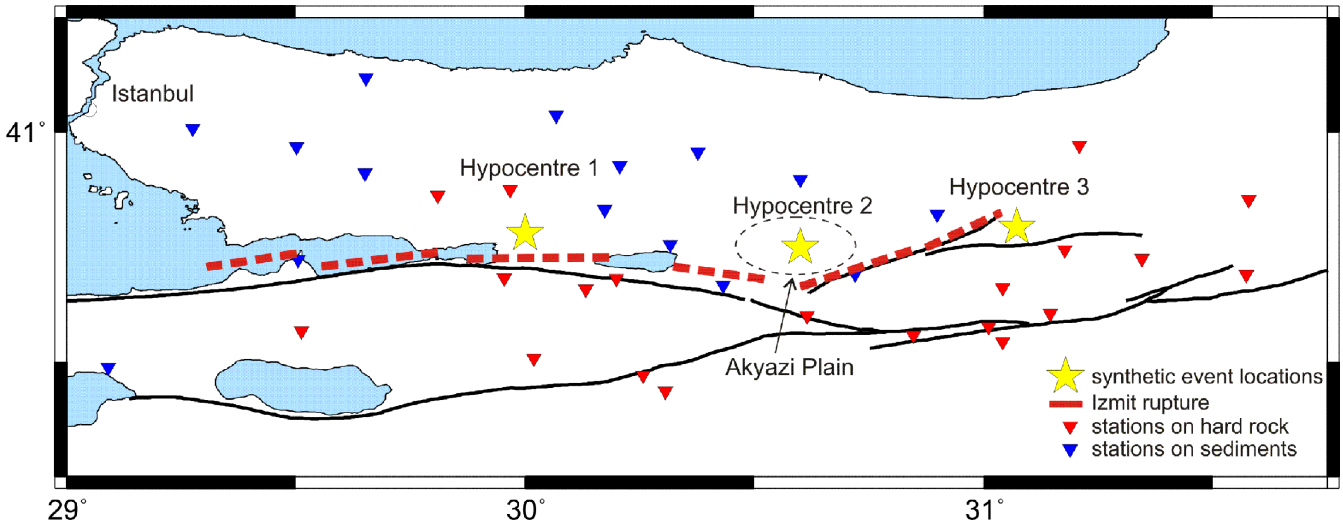

Figure 1. Configuration of stations of the seismic network deployed along the 1999 $M_w = 7.4$ rupture of the North Anatolian Fault Zone to monitor its aftershock activity (Baumbach *et al*. 2003). The stars mark the locations of the events considered in the synthetic tests. Red triangles represent stations on sediments and blue triangles represent stations on hard rock. Fault lines are taken from the Turkey General Directorate of Mineral Research and Exploration and red dashed lines are surface ruptures of the 1999 Izmit earthquake observed by Barka *et al*. (2002).

Synthetic resolution studies of non-DC components have been published in several papers. For example, Vavryčuk (2007) studied numerically the errors in the non-DC mechanisms for microearthquakes from synthetic borehole data with various configurations of boreholes, and Šílený (2009) performed a synthetic case study testing the resolution capability of non-DC mechanisms for microearthquakes at a station configuration simulating the geothermal site at Soultz-sous-Forets, France. The latter author showed that even low non-DC components were well resolved not being masked by spurious non-DC components when *P*- and *S*-wave amplitudes are inverted for the full moment tensor.

In contrast to previous studies dealing with microseismicity observed at local networks (<10 km), we focus on the resolution capability of regional networks (aperture ~220 km) with configurations designed typically for monitoring aftershock sequences of large ($M > 7$) earthquakes. In addition, we test two different moment tensor inversion techniques: First, we perform a standard linear inversion for the full moment tensor, and secondly, a non-linear moment tensor inversion constrained to a shear-tensile (also called tensile or dislocation) source model is used. Here, we have to emphasize that the latter method is only applicable to real observations, provided the data are consistent with the shear-tensile source model (Vavryčuk 2001; Minson *et al*. 2007; Vavryčuk 2011). The consistency of this model can be verified, for example, by evaluating the consistency factor proposed by Vavryčuk (2011, eq. 23). However, for both methods we test two different sets of input data: *P*- and *S*-wave amplitudes or *P*-wave amplitudes only. As a case study we simulate seismic observations of aftershocks of the 1999 $M_w = 7.4$ Izmit earthquake in northwestern Turkey and determine the resolution limits for their non-DC components. We model synthetic seismic recordings of aftershocks adopting several source types of shear-tensile faulting (Vavryčuk 2001). To simulate real data, we contaminate the synthetic waveforms with random noise. We also use inaccurate hypocentre locations and velocity models when determining the Green's functions needed for the inversion. Finally, we investigate the resolution of source related non-DC components in dependence of the linear and non-linear inversion approach as well as the input data *P*- and *S*-wave amplitudes. The application to real observations is presented in a companion paper (Stierle *et al* 2014).

2 SETUP OF THE EXPERIMENT AND METHODS

As an example of regional network data, we adopt observations of aftershocks of the 1999 $M_w = 7.4$ Izmit earthquake. The Izmit earthquake ruptured a ~140-km-long segment of the North Anatolian Fault Zone (NAFZ hereafter) in NW Turkey (e.g. Tibi *et al*. 2001; Barka *et al*. 2002). To monitor its aftershock activity, a network of 35 three-component short-period seismic stations was completed within 4 d after the main shock covering the entire rupture (Baumbach *et al*. 2003; Fig. 1). The aperture of the network is about 220 km and seismicity mainly occurred in a depth range between 6 and 16 km (Bulut *et al*. 2007). Aftershock focal mechanisms around the Izmit epicentre and at the eastern part of the rupture indicate dominantly strike-slip motions with some normal faulting components. In contrast, below the Akyazi Plain at the central part of the rupture, where a substantial slip deficit was accumulated during the main shock, events reflect purely EW-extensional normal faulting indicating a small pull-apart structure (Bohnhoff *et al*. 2006). This region can be seen as a potential area where significant non-DC components might exist.

For our synthetic case study, we choose three different hypocentres (1–3) with a focal depth of 11 km, representing spots of pronounced Izmit aftershock activity and located close to the main fault along the rupture (Fig. 1). Synthetic amplitudes are calculated adopting a shear-tensile source model (Vavryčuk 2001; Fig. 2), where slope angle α controls the non-DC content of the source mechanism (Table 1). For each hypocentre we modelled nine strike-slip (strike = 0°, dip = 90°, rake = 180°) events and nine EW-extensional normal faulting (strike = 0°, dip = 45°, rake = −90°) events with combined shear-tensile source mechanisms, where α is ranging from 0° to 20° (Table 1). In total, 54 events with different locations and focal mechanisms were simulated.

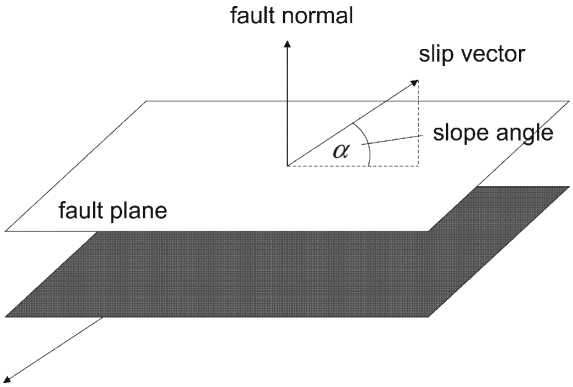

Figure 2. Shear-tensile source model. The non-DC content of the source mechanism is controlled by the slope angle α ($\alpha = 0°$ is for pure shear slip and $\alpha = 90°$ is tensile faulting).

Table 1. Percentages of the non-DC components in the seismic moment tensor of the shear-tensile source with varying slope α. The decomposition by Vavryčuk (2001) is used.

Alpha (°)	0	2.5	5	7.5	10	12.5	15	17.5	20
Non-DC (per cent)	0	12.1	22.2	30.9	38.5	44.6	50.1	54.8	60

Bulut *et al*. (2007) presented a 1-D *P*-wave velocity model for the Izmit area derived from recordings of the aftershock sequence of the 1999 Izmit earthquake. Koulakov *et al*. (2010) further determined *S*-wave velocities as well as v_P/v_S ratios for the Izmit area using aftershocks of the Izmit earthquakes. Since stations are situated partly on hard rock and partly on a shallow sediment layer (Parolai *et al*. 2004), two different sets of path-specific 1-D velocity models are used for computing synthetic amplitudes: One set of velocity models representing stations situated on a shallow sediment layer and one set of velocity models for stations deployed on hard rock (Fig. 3, red and black lines, respectively). The velocity models in each set vary within the first 5 km by ±15 per cent (see Fig. 3).

Based on the 35-station seismic network, we selected a subset of 22 stations for each hypocentre representing a realistic number of stations recording an event (Fig. 4) of magnitude 3. We find that all three coverages suffer from a rather poor distribution of stations at the centre of the focal sphere. In particular, near vertical directions are missing because of absence of stations at small epicentral distances (less than 15–20 km). This deficiency is inherent to all regional networks of a similar aperture being a compromise between demands on covering a large seismically active region and deploying a limited number of stations.

Synthetic *P*- and *S*-wave amplitudes A^{syn} were calculated from prescribed moment tensor **M** and the spatial derivatives of the Green's function **G** using the representation theorem. Because we use a point-source approximation and invert amplitudes, the space–time convolution integral is reduced to a simple multiplication

$$A_i^{syn} = M_{nk} \cdot G_{in,k}, \qquad (1)$$

where subscript i is the sequential number of the station. As mentioned earlier, the moment tensor was determined adopting the shear-tensile source model after Vavryčuk (2001). To compute Green's functions, we used ray tracing techniques in a smoothed velocity model (Fig. 3) after Červený (2001). The smoothed velocity model is necessary to ensure valid rays and to avoid caustic points, which produce artificially high amplitudes. The effect of the Earth's surface was incorporated in the Green's functions. Using ray tracing techniques, we obtained amplitudes corresponding to amplitudes of the direct *P* and *S* waves at each station of the network. For clarity, no waveform modelling is done and thus no picking of amplitudes was necessary for the synthetic tests.

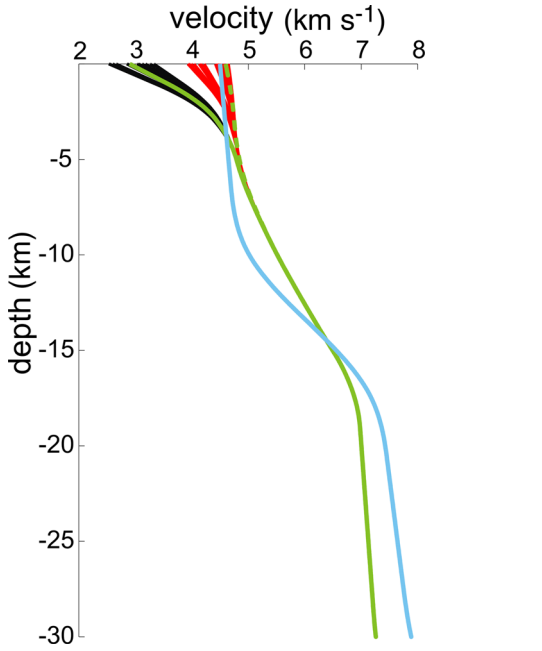

Figure 3. Smoothed velocity models used for the synthetic tests. Two different sets of velocity models were used for modelling synthetic amplitudes: with a shallow sediment layer (red lines) and without sediments (black lines). The models within one set differ from each other by approximately ±15 per cent within the first 5 km. Model 1 (green solid line), model 2 (green dashed line) and model 3 (blue solid line) were used for simulating errors in the velocity structure.

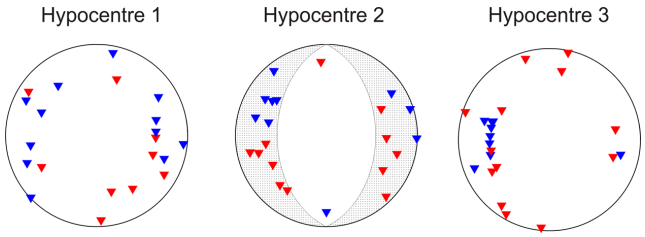

Figure 4. Station coverage on the focal sphere for a selected subset of 22 stations at the three hypocentres shown in Fig. 1. Blue triangles are stations on sediments and red triangles are stations on hard rock. The focal sphere coverage is unfavourable for normal faulting mechanisms since the stations are located close to the nodal lines and therefore the *P*-wave amplitudes are small and more sensitive to errors.

After completing the pool of synthetic amplitudes, the full moment tensor inversion was performed. Prior to the inversion, amplitudes were weighted using two different scales. First, *S*-wave amplitudes were weighted by 0.5, because they are more difficult to pick and thus have higher uncertainties. Second, amplitudes measured at stations with epicentral distances smaller than 30 km were weighted by value of 1 and the remaining by value of 0.5. Since the signal at stations with large epicentral distance is usually weak and waves are more scattered and disturbed by noise and attenuation, picked amplitudes have generally less accuracy and are not as reliable as amplitudes at closer stations.

We introduce three different types of errors in the moment tensor inversion in order to analyse the sensitivity of non-DC

components. First, the influence of uniformly distributed random noise was tested by a repeated inversion of amplitudes, where the noise level was station and distance dependent. In total, 100 realizations per event were performed. Second, the hypocentre was shifted by 2 km downwards and 2.5 km laterally with respect to its true position. These values represent the absolute location errors of the Izmit aftershocks (Bulut *et al*. 2007). Third, inaccuracies in the velocity model were introduced when computing Green's functions to simulate poor knowledge of the geological structure. By using only one model for stations on hard rock (model 2, Fig. 3) and one model for stations on sediments (model 1, Fig. 3), we characterized low errors. To simulate higher errors in the velocity structure, we used one velocity model for all stations (model 3, Fig. 3).

The full moment tensor was determined by the generalized linear inversion (e.g. Lay & Wallace 1995) of direct *P*- and *S*-wave amplitudes:

$$\mathbf{M} = \mathbf{G}^{-g}\mathbf{A} \quad \text{with} \quad \mathbf{G}^{-g} = [\mathbf{G}^{\mathrm{T}}\mathbf{G}]^{-1}\mathbf{G}^{\mathrm{T}}, \tag{2}$$

where **M** is the full moment tensor, **G** is the matrix of spatial derivatives of the Green's function and **A** is the vector of observed amplitudes.

The moment tensor constrained to a shear-tensile source model was assessed via grid search by minimizing the L2 norm between observed and theoretical amplitudes. Using this approach the angles of the tensile source can directly be derived from the observed wavefield (Vavryčuk 2011). Furthermore, the compensated linear vector dipole (CLVD) and isotropic (ISO) component are linearly dependent. They always have the same sign and their ratio is constant and depends on the v_P/v_S ratio in the source area (see Vavryčuk 2001, 2011):

$$\frac{ISO}{CLVD} = \frac{3}{4}\left(\frac{v_P}{v_S}\right)^2 - 1, \tag{3}$$

where ISO and CLVD mean the percentages calculated as follows:

$$\mathrm{ISO} = \frac{1}{3}\frac{\mathrm{trace}(\mathbf{M})}{|M_{|\max|}|}100 \text{ per cent}$$

$$\mathrm{CLVD} = -2\frac{M^*_{|\min|}}{M^*_{|\max|}}\left[100 \text{ per cent} - |\mathrm{ISO}|\right]. \tag{4}$$

Tensor **M** is the full moment tensor, and $M_{|\min|}$ and $M_{|\max|}$ are the eigenvalues of **M** with the minimum and maximum absolute value, respectively. Analogously, we define the eigenvalues for the deviatoric part $\mathbf{M}^*$ of the moment tensor **M**. Eq. (3) implies that the errors of ISO and CLVD components are linked linearly and thus we obtain a similar accuracy for both.

Both inversions use ray tracing techniques in a smoothed velocity model and they incorporate calculation of ray-theoretical Green's functions (Červený 2001). Basically, here we use the same procedure as for determining synthetic amplitudes. To assess the quality of the retrieved moment tensors, the normalized root-mean-square (rms) error between theoretical and observed amplitudes is determined using the following formula:

$$\mathrm{rms} = \frac{\sqrt{\sum_{i=1}^{N}\left(A_i^{\mathrm{obs}} - A_i^{\mathrm{theo}}\right)^2}}{\sqrt{\sum_{i=1}^{N}\left(A_i^{\mathrm{obs}}\right)^2}}, \tag{5}$$

where A^{obs} and A^{theo} are the observed and theoretical amplitudes, respectively, subscript i is the sequential number of the station and N is the total number of stations at which the amplitudes were recorded for the respective event. The decomposition of the moment tensor into the percentage of the DC and non-DC components is performed after Vavryčuk (2001), where the non-DC component consists of a CLVD and an ISO component.

To analyse the accuracy of the retrieved source mechanisms and the resolution of the non-DC components, we use two criteria. First, theoretical and retrieved non-DC components are compared. Here, we analyse the absolute errors between retrieved and theoretical non-DC components. Therefore, a change in the polarity of ISO and CLVD components might appear as a minimum in the corresponding figure (for example, Fig. 7d, blue dashed line). Second, the deviation of *P*- and *T*-axes between the theoretical and retrieved DC mechanism is analysed to investigate the stability of the orientation of the fault plane. The angles between theoretical and retrieved *P*- and *T*-axes are calculated using the scalar product of their direction vectors (e.g. Kagan 1991).

3 RESULTS OF THE SYNTHETIC EXPERIMENT AND DISCUSSION

In the following, we discuss the results for Hypocentre 2 (Fig. 1). Similar conclusions are drawn for hypocentres 1 and 3 and obtained results for these are shown in the Supporting Information.

We started with contaminating the amplitudes with random noise. The noise level depends on the epicentral distance and was ranging from 10 to 25 per cent. It was further increased by 5 per cent for stations deployed on a sediment layer. The misfit of amplitudes measured by the rms error was less than 0.15, which represents a good fit of amplitudes. Standard deviations for the ISO and CLVD components as well as the deviation of *P*- and *T*-axes are shown in Figs 5(a)–(c) for the inversion of *P*-wave amplitudes only and in Figs 6(a)–(c) for the inversion of *P*- and *S*-wave amplitudes. The orientation of the fault plane is well resolved in most cases regardless of the input data or type of inversion with deviations of *P*- and *T*-axes smaller than 8° (Figs 5c and 6c). Furthermore, we observe that errors in the ISO component are slightly higher for the full moment tensor inversion (∼2 per cent) than for the constraint inversion (∼1 per cent) when the *P* and *S* amplitudes are inverted. This difference is more significant for the inversion of only *P*-wave amplitudes, where the error is 7 per cent for the full moment tensor inversion and 3 per cent for the constraint inversion. Also the errors for the CLVD are about two to three times higher for the full moment tensor inversion of *P*- and *S*-wave amplitudes than for the constrained inversion. When inverting only *P*-wave amplitudes for the full moment tensor, the error in the CLVD component remarkably increases and it is as high as 30 per cent, whereas errors remain smaller than 10 per cent when the constrained inversion is applied. The observation that errors mainly affect the CLVD component in the full moment tensor inversion has been observed previously (Vavryčuk 2011). The origin of such observation lies in the decomposition of the moment tensor into its CLVD and ISO percentages. The CLVD component is calculated from the ratio between the lowest and highest eigenvalues of the deviatoric moment tensor (see eq. 4) and this non-linear relation makes the CLVD more sensitive to inaccuracies of the inverted moment tensor. In contrary, the relation between the ISO and the eigenvalues of the moment tensor is linear and therefore robust against the errors. Hence, the ISO component is, in general, less sensitive to errors in the modelling procedure and can be better resolved than the CLVD component. In the constrained inversion, however, the CLVD and ISO components are

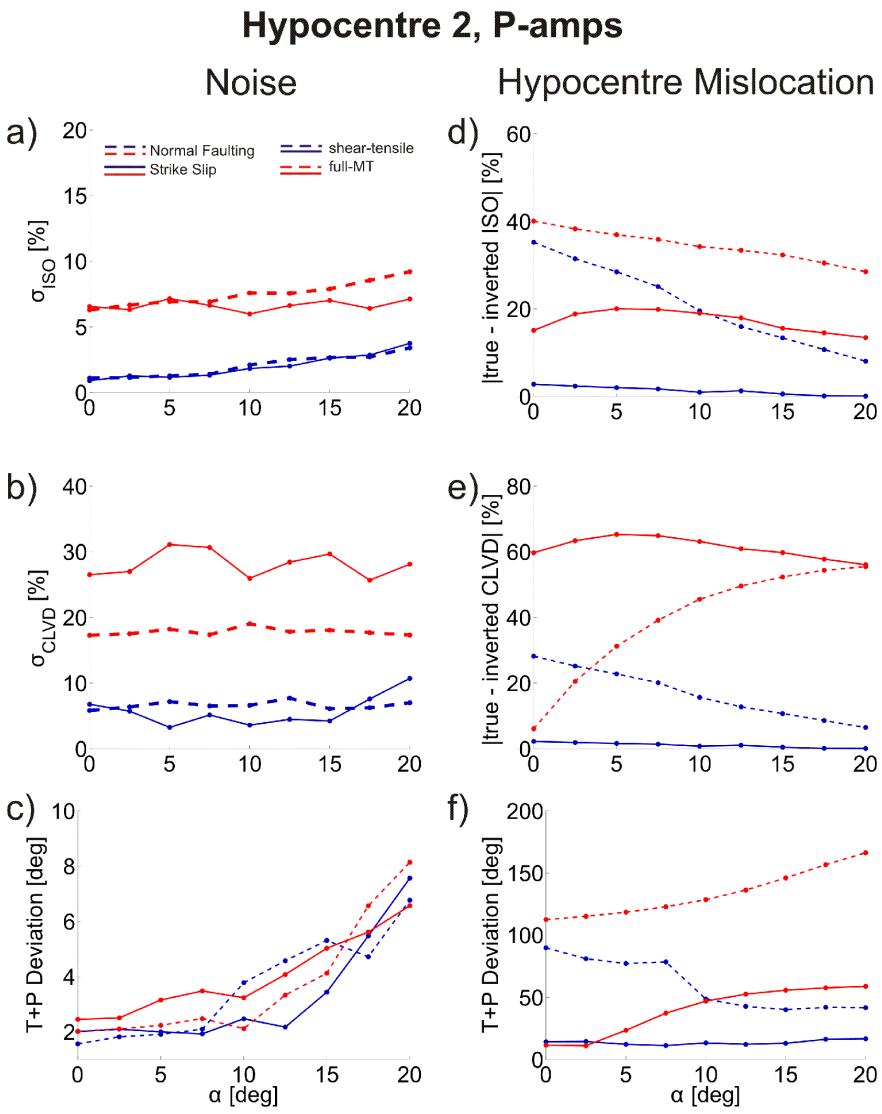

Figure 5. Moment tensor inversion for noisy amplitudes (left-hand side) and hypocentre mislocation (right-hand side) for the inversion of *P*-wave amplitudes only at Hypocentre 2. Errors are shown as a function of slope α. Red lines—the linear full moment tensor inversion, blue lines—the non-linear inversion constrained to a shear-tensile source model. We further distinguish between strike-slip mechanism (solid lines) and normal faulting mechanisms (dashed lines). Plots (a) and (b) show standard deviations of the ISO and CLVD components, respectively, determined from 100 inversions of noise contaminated amplitudes. Plots (d) and (e) present the difference between the retrieved and true percentages of ISO and CLVD components, respectively. The deviation between the retrieved and true *P*- and *T*-axes are displayed in plots (c) and (f).

linearly dependent (Vavryčuk 2001, 2011) and therefore the errors in the CLVD component are clearly reduced. Here, the error is about three times smaller than for the full moment tensor inversion.

Next, we incorporated errors in the hypocentre location. Results are shown in Figs 5(d)–(f) and 6(d)–(f) for the inversion of *P*-wave amplitudes only and of *P*- and *S*-wave amplitudes, respectively. Although we were able to achieve good fits between theoretical and inverted amplitudes with an rms error less than 0.25 the influence on the resolution of non-DC components is considerable. Errors in the non-DC components can be up to 15 per cent when *P*- and *S*-wave amplitudes are inverted. When inverting only *P*-wave amplitudes, the errors are two to three times larger. Thus, real non-DC components can easily be masked by spurious non-DC components. Here, including the *S*-wave amplitudes is very important to obtain sufficiently small errors in the non-DC components in order to be able to discriminate between spurious and real non-DC components.

Furthermore, we observed that normal faulting mechanisms are more sensitive to modelling errors reflecting higher errors in the ISO and CLVD components than strike-slip mechanisms. The reason for this is the unfavourable distribution of stations on the focal sphere for the EW-extensional normal faulting mechanism, because most stations are located close to nodal lines (Fig. 4). Consequently, the *P*-wave amplitudes are small and thus more sensitive to errors.

The orientations of *P*- and *T*-axes show rotations of about 20° for both inversion methods applied to *P*- and *S*-wave amplitudes (Fig. 6f). Inverting only *P*-wave amplitudes, rotations of *P*- and *T*-axes are quite significant and normal faulting mechanisms might even be misinterpreted as a strike-slip mechanism (Fig. 5f). This confirms again that including *S*-wave amplitudes is very important for the accurate determination of the orientation of *P*- and *T*-axes.

Finally, we simulated inaccuracies in the velocity structure. First, model 1, representing stations on sediments, and model 2, used for stations on hard rock, were used to represent weak errors in the

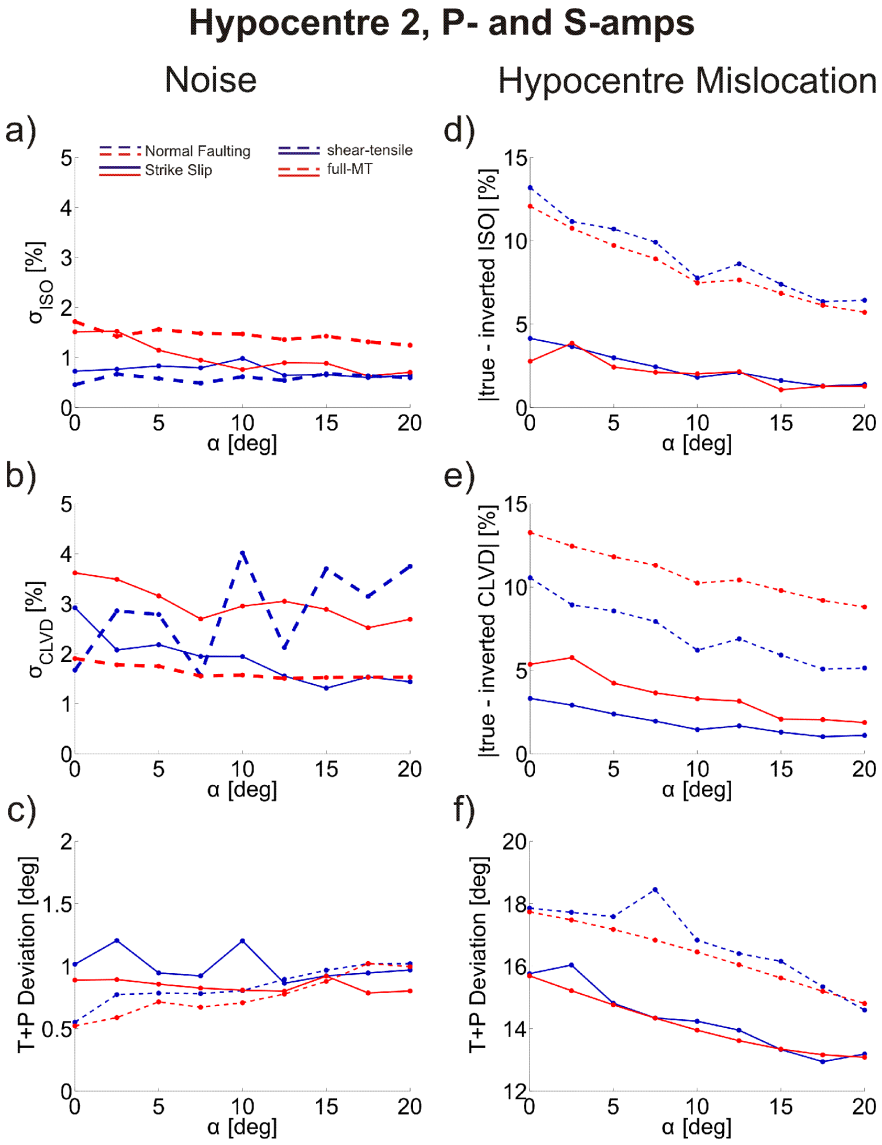

Figure 6. Moment tensor inversion for noisy amplitudes (left-hand side) and hypocentre mislocation (right-hand side) for the inversion of *P*- and *S*-wave amplitudes at Hypocentre 2. For details, see the caption of Fig. 5.

velocity structure. Observed rms errors are around 0.1 and results for the inversion of *P*-wave amplitudes only and of *P*- and *S*-wave amplitudes are shown in Figs 7 and 8, respectively. Here, we found small errors in non-DC components being up to ±6 per cent for the inversion of *P*- and *S*-wave amplitudes. Deviations for *P*- and *T*-axes are 2° or smaller. The errors in the non-DC components significantly increase when only *P*-wave amplitudes are inverted and also the fault plane can considerably rotate. We further found that the constraint inversion is substantially more stable than the full moment tensor inversion especially when only the *P*-wave amplitudes are inverted.

Secondly, we further incorporate higher errors in the velocity structure by using only one velocity model common for all stations (model 3, Fig. 3). This leads to rms errors around 0.2. As expected, errors in the non-DC components are higher being up to ±13 per cent for the inversion of *P*- and *S*-wave amplitudes and up to ±80 per cent for the inversion of only *P*-wave amplitudes. However, the orientation of *P*- and *T*-axes is stable when the *P*- and *S*-wave amplitudes are inverted with a rotation smaller than 10°. Here, the errors in the non-DC components and in the deviation of the *P*- and *T*-axes are similar to the errors introduced by the hypocentre mismodelling. However, inverting only the *P*-wave amplitudes is resulting in rotations of the *P*- and *T*-axes as high as 100°.

Interestingly, we further observe significant variations of errors in dependence on source mechanisms. Errors in the non-DC components of normal faulting mechanisms are at least two to three times higher than those for the strike-slip mechanisms. Furthermore, the errors are decreasing when the percentage of non-DC components is increasing so that tensile normal faulting mechanisms are less sensitive to errors in the velocity structure than pure shear mechanisms. This may be explained by the radiation pattern. The radiation pattern is quadrant for a pure shear source but axially symmetric for a pure tensile source, which is therefore less dependent on directions. Errors in the velocity structure imply ray deviations, which are less damaging for the tensile crack than for the shear slip. Although the radiation pattern of a shear-tensile slip with slope of 20° is still far from an axial symmetry, it is less sensitive to ray deviations than shear slip sources.

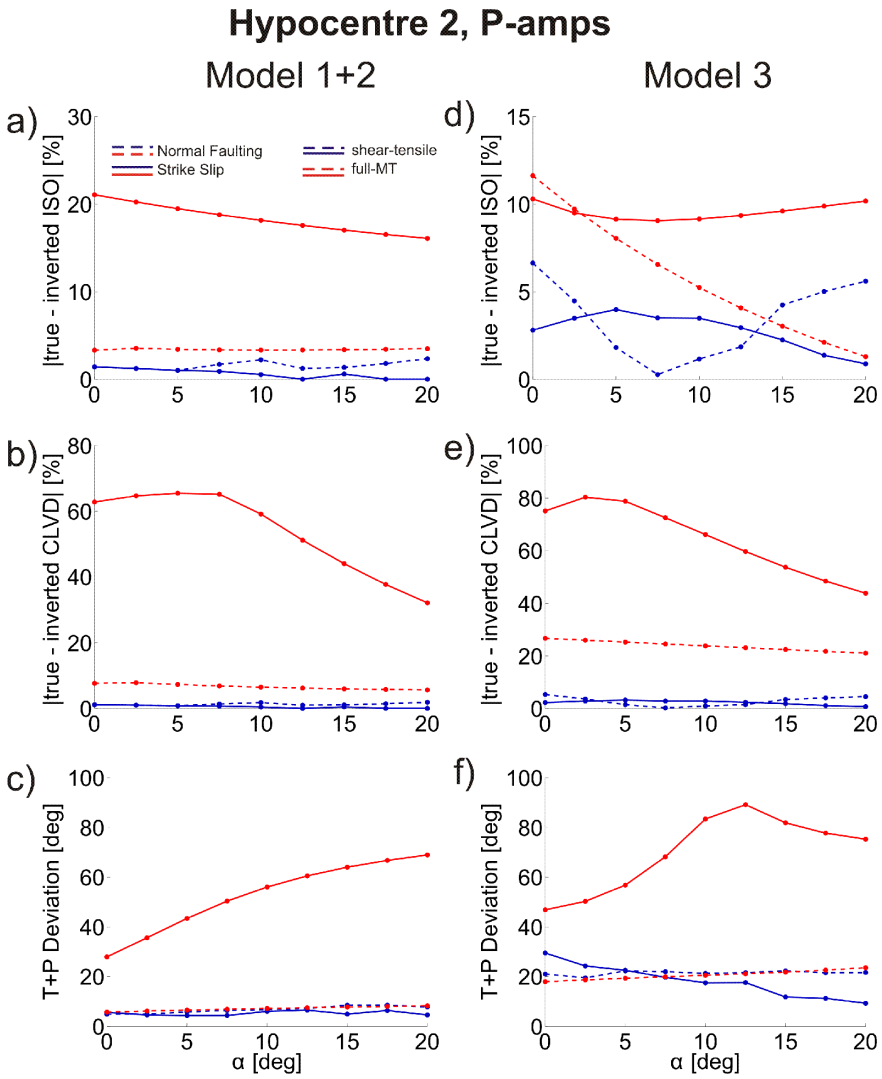

Figure 7. Moment tensor inversion for weak (left-hand side) and strong (right-hand side) velocity mismodelling using *P*-wave amplitudes only at Hypocentre 2. Plots (a) and (b) show the difference between the retrieved and true percentages of ISO and CLVD components, respectively, using model 1+2. Plots (d) and (e) show the same for model 3. The deviations between the *P*- and *T*-axes of the retrieved and true fault planes are displayed in plots (a) and (f) for models 1+2 and model 3, respectively.

Finally, we performed tests combining noise contamination, errors in the hypocentre location and inaccuracies in the velocity structure. Noise and errors in the hypocentre location were realized as described above and for simulating the errors in the velocity structure we used model 3 (Fig. 3) for all stations. We found that the errors remain below ±15 per cent. Thus, the errors do not cumulate, but remain below the error limits, which are observed when the hypocentre mislocation, velocity mismodelling and noise are considered separately.

4 CONCLUSIONS

We tested two different moment tensor inversions to analyse their ability to resolve source related non-DC components in regional network data: a linear full moment tensor inversion, and a non-linear inversion constrained to a shear-tensile source model. Adopting a shear-tensile source model, we simulated seismic observations from a regional 35-station seismic network deployed along the rupture of the 1999 $M_w = 7.4$ Izmit earthquake for monitoring its aftershocks. Based on this synthetic experiment, we arrived at the following conclusions:

(i) The constrained inversion yields smaller errors in non-DC components especially for the CLVD component. Here, the errors are two to 15 times smaller than for the full moment tensor inversion. The full moment tensor might be a too detailed description of a tectonic source and therefore it can be unstable, if the data quality is low or the velocity structure is poorly known. Constraining the parameter space by the shear-tensile source model reduces the number of possible source mechanisms and non-physical solutions such as explosions or implosions are excluded from the beginning. This makes the inversion much more stable and robust against errors. When real observations of tectonic events are consistent with the shear-tensile source model, such as, for example, aftershocks of the 1999 Izmit earthquake (Stierle *et al*. 2014), we recommend applying the non-linear inversion constraint to the shear-tensile source model, since the errors in the non-DC components can clearly be reduced.

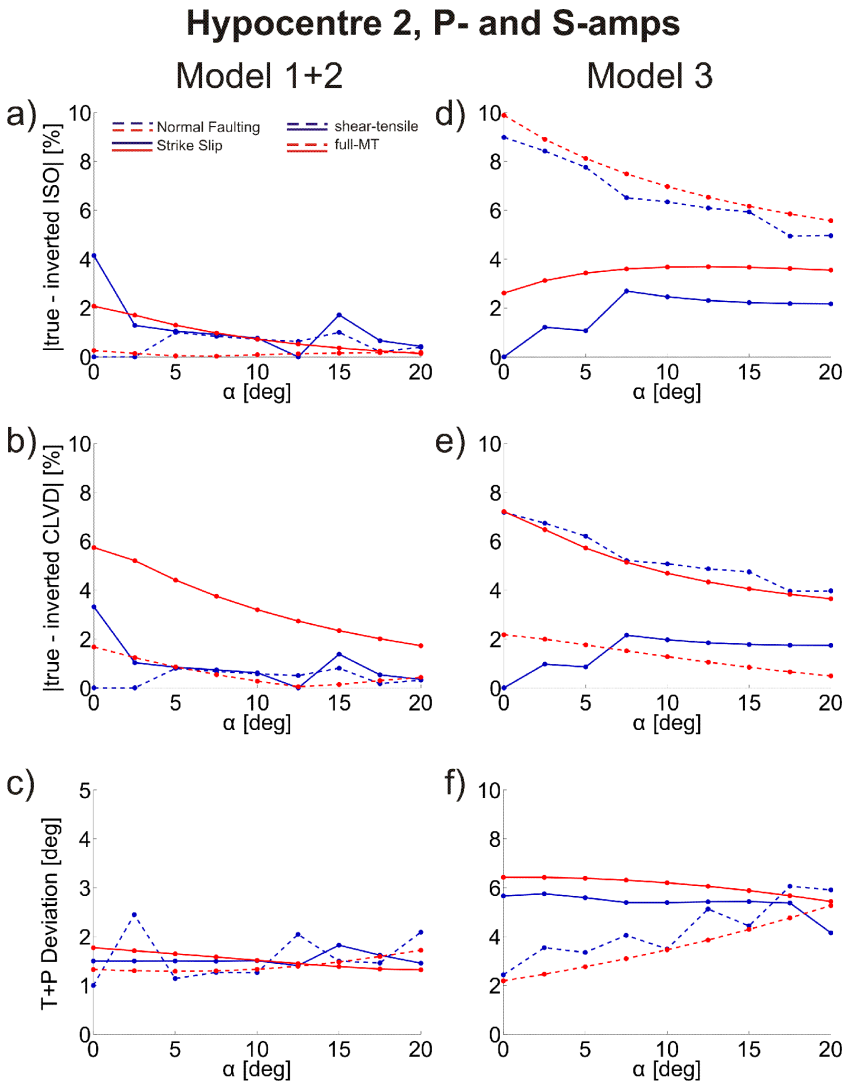

Figure 8. Moment tensor inversion for weak (left-hand side) and strong (right-hand side) velocity mismodelling using *P*- and *S*-wave amplitudes at Hypocentre 2. For details, see the caption of Fig. 7.

(ii) Retrieving non-DC components from regional seismic networks equipped by short-period stations with apertures in the range of 200–300 km and with station spacing of 20–30 km is particularly difficult due to the lack of observations from stations at epicentral distances less than 15–20 km. This causes irregular focal sphere coverage where near vertical directions are missing.

(iii) The inversion of *P*-wave amplitudes alone is not, in general, sufficient for a reliable determination of the non-DC components when using data from regional networks. Therefore, it is necessary to incorporate both, *P*- and *S*-wave amplitudes into the inversion.

(iv) The ISO component is usually less sensitive to errors than the CLVD component when the full moment tensor inversion is applied. This is well explained by properties of the moment tensor decomposition: the ISO component is a linear function while the CLVD component is a non-linear function of eigenvalues of the moment tensor. In contrary, the inversion constrained to a shear-tensile source model links the ISO and CLVD components and the CLVD errors are reduced and thus determined more precisely than for the full moment tensor inversion.

(v) Even for a network geometry as good as that used for observing the Izmit aftershocks the error bounds of retrieved non-DC components remain considerable. Assuming realistic errors in the modelling procedure, we are able to detect only significant source–related ISO and CLVD components (larger than ±15 per cent). Smaller non-DC components cannot be resolved since the amount of spurious non-DC components can be up to ±15 per cent. However, the expected non-DC components in Izmit aftershocks might be substantially larger given, for example, the extensional settings below the Akyazi Plain.

(vi) Deviations of *P*- and *T*-axes between retrieved and modelled mechanisms are smaller than 15° when *P*-and *S*-wave amplitudes are inverted. Thus, the orientation of *P*- and *T*-axes can be determined precisely even when errors in modelling procedures are high.

(vii) When aiming at detecting potential non-DC components by a regional seismic network, we suggest carrying out studies as this one prior to the deployment. Šílený 2009, for example, showed that the network geometry is in particular important when aiming to resolve spurious non-DC components. A carefully designed geometry of seismic network can significantly increase the potential of the network to analyse the DC and non-DC components in the seismic moment tensors and thus bring new information on seismic source processes in the region of interest.

ACKNOWLEDGEMENTS

This work was supported by the German Research Foundation (DFG) under the contract Bo1877/1-1, and by the Grant Agency of the Czech Republic, Grant No. P210/12/1491 and Grant No. P210/12/2235. We acknowledge funding from the Helmholtz Association within the Young Investigator Group 'From microseismicity to large earthquakes'. The first author E. Stierle thanks the Christiane-Nüsslein-Volhard Foundation for cofunding. We thank the editor Yehuda Ben-Zion and acknowledge comments by Sean Ford and Zacharie Duputel.

REFERENCES

Barka, A. *et al.*, 2002. The surface rupture and slip distribution of the 17 August 1999 Izmit earthquake (*M* 7.4), North Anatolian fault, *Bull. seism. Soc. Am.,* **92**(1), 43–60.

Baumbach, M. *et al.*, 2003. Calibration of an ML scale in northwestern Turkey from 1999 Izmit aftershocks, *Bull. seism. Soc. Am.,* **93,** 2289–2295.

Ben-Zion, Y. & Ampuero, J.-P., 2009. Seismic radiation from regions sustaining material damage, *Geophys. J. Int.,* **178,** 1351–1356.

Bohnhoff, M., Grosser, H. & Dresen, G., 2006. Strain partitioning and stress rotation at the North Anatolian fault zone from aftershock focal mechanisms of the 1999 Izmit *M*w=7.4 earthquake, *Geophys. J. Int.,* **166,** 373–385.

Bulut, F., Bohnhoff, M., Aktar, M. & Dresen, G., 2007. Characterization of aftershock-fault plane orientations of the 1999 Izmit (Turkey) earthquake using high-resolution aftershock locations, *Geophys. Res. Lett.,* **34**(20), L20306, doi:10.1029/2007GL031154.

Červený, V., 2001. *Seismic Ray Theory,* Cambridge Univ. Press.

Frohlich, C., 1994. Earthquakes with non-double-couple mechanisms, *Science,* **264,** 804–809.

Horálek, J., Šílený, J. & Fischer, T., 2002. Moment tensors of the January 1997 earthquake swarm in NW Bohemia (Czech Republic): double-couple vs. non-double-couple events, *Tectonophysics,* **356**(1), 65–85.

Julian, B.R., Miller, A.D. & Foulger, G.R., 1998. Non-double-couple earthquakes, 1. Theory, *Rev. Geophys.,* **36,** 525–549.

Kagan, Y.Y., 1991. 3-D rotation of double-couple earthquake sources, *Geophys. J. Int.,* **106**(3), 709–716.

Koulakov, I., Bindi, D., Parolai, S., Grosser, H. & Milkereit, C., 2010. Distribution of seismic velocities and attenuation in the crust beneath the North Anatolian Fault (Turkey) from local earthquake tomography, *Bull. seism. Soc. Am.,* **100**(1), 207–224.

Kravanja, S., Panza, G.F. & Šílený, J., 1999. Robust retrieval of a seismic point source time function, *Geophys. J. Int.,* **136,** 385–394.

Lay, T. & Wallace, T.C., 1995. *Modern Global Seismology,* Academic Press.

Miller, A.D., Foulger, G.R. & Julian, B.R., 1998. Non-double-couple earthquakes, 2. Observations, *Rev. Geophys.,* **36,** 551–568.

Minson, S.E., Dreger, D.S., Bürgmann, R., Kanamori, H. & Larson, K.M., 2007. Seismically and geodetically determined nondouble-couple source mechanisms from the 2000 Miyakejima volcanic earthquake swarm, *J. geophys. Res.,* **112,** B10308, doi:10.1029/2006JB004847.

Panza, G.F. & Sarao, A., 2000. Monitoring volcanic and geothermal areas by full seismic moment tensor inversion: are non-double-couple components always artefacts of modelling? *Geophys. J. Int.,* **143**(2), 353–364.

Parolai, S., Bindi, D., Baumbach, M., Grosser, H., Milkereit, C., Karakisa, S. & Zunbul, S., 2004. Comparison of different site response estimation techniques using aftershocks of the 1999 Izmit earthquake, *Bull. seism. Soc. Am.,* **94**(3), 1096–1108.

Rößler, D., Krüger, F. & Rümpker, G., 2007. Retrieval of moment tensors due to dislocation point sources in anisotropic media using standard techniques, *Geophys. J. Int.,* **169**(1), 136–148.

Rößler, D., Krüger, F., Psenčík, I. & Rümpker, G., 2008. Retrieval of source parameters of an event of the 2000 West Bohemia earthquake swarm assuming an anisotropic crust, *Stud. Geophys. Geod.,* **52**(2), 285–286.

Šílený, J., 2009. Resolution of non-double-couple mechanisms: simulation of hypocentre mislocation and velocity structure mismodeling, *Bull. seism. Soc. Am.,* **99,** 2265–2272.

Stierle, E., Bohnhoff, M. & Vavryčuk, V., 2014. Resolution of non-double-couple components in the seismic moment tensor using regional networks: II. Application to aftershocks of the 1999 Mw 7.4 Izmit earthquake, *Geophys. J. Int.,* doi:10.1093/gji/ggt503.

Tibi, R. *et al.*, 2001. Rupture processes of the 1999 August 17 Izmit and November 12, Düzce (Turkey) earthquakes, *Geophys. J. Int.,* **144**(2), F1–F7.

Vavryčuk, V., 2001. Inversion for parameters of tensile earthquakes, *J. geophys. Res.,* **106**(16), 16 339–16 355.

Vavryčuk, V., 2007. On the retrieval of moment tensors from borehole data, *Geophys. Prospect.,* **55,** 381–391.

Vavryčuk, V., 2011. Tensile earthquakes: theory, modeling, and inversion, *J. geophys. Res.,* **116**(B12), B12320, doi:10.1029/2011JB008770.

SUPPORTING INFORMATION

Additional Supporting Information may be found in the online version of this article:

Figure S1. Moment tensor inversion for noisy amplitudes (left-hand side) and hypocentre mislocation (right-hand side) for the inversion of *P*-wave amplitudes only at Hypocentre 1.
Figure S2. Moment tensor inversion for noisy amplitudes (left-hand side) and hypocentre mislocation (right-hand side) for the inversion of *P*-wave amplitudes only at Hypocentre 3.
Figure S3. Moment tensor inversion for noisy amplitudes (left-hand side) and hypocentre mislocation (right-hand side) for the inversion of *P*- and *S*-wave amplitudes at Hypocentre 1.
Figure S4. Moment tensor inversion for noisy amplitudes (left-hand side) and hypocentre mislocation (right-hand side) for the inversion of *P*- and *S*-wave amplitudes at Hypocentre 3.
Figure S5. Moment tensor inversion for weak (left-hand side) and strong (right-hand side) velocity mismodelling using *P*-wave amplitudes only at Hypocentre 1.
Figure S6. Moment tensor inversion for weak (left-hand side) and strong (right-hand side) velocity mismodelling using *P*-wave amplitudes only at Hypocentre 3.
Figure S7. Moment tensor inversion for weak (left-hand side) and strong (right-hand side) velocity mismodelling using *P*- and *S*-wave amplitudes at Hypocentre 1.
Figure S8. Moment tensor inversion for weak (left-hand side) and strong (right-hand side) velocity mismodelling using *P*- and *S*-wave amplitudes at Hypocentre 3.
(http://gji.oxfordjournals.org/lookup/suppl/doi:10.1093/gji/ggt502/-/DC1)

Please note: Oxford University Press are not responsible for the content or functionality of any supporting materials supplied by the authors. Any queries (other than missing material) should be directed to the corresponding author for the article.